14, 2283 (1975); R. W. Pastor, R. M. Venable, M. Karplus, *J. Chem. Phys.* **89**, 1112 (1988); R. W. Pastor, R. M. Venable, M. Karplus, *Proc. Natl. Acad. Sci. U.S.A.* **88**, 892 (1991).
13. B. J. Hardy and R. W. Pastor, *J. Comput. Chem.*, in press.
14. A. Seelig and J. Seelig, *Biochemistry* **13**, 4839 (1974).
15. R. P. Rand and V. A. Parsegian, *Biochim. Biophys. Acta* **998**, 351 (1989).
16. R. W. Pastor and R. M. Venable, in *Computer Simulation of Biomolecular Systems: Theoretical and Experimental Applications*, W. F. van Gunsteren, P. K. Weiner, A. K. Wilkinson, Eds. (ESCOM Science Publishers, Leiden, in press).
17. The membrane system contained 72 lipid molecules and 2533 water molecules for a total of 16,893 atoms (including hydrogens). Dimensions imposed for three-dimensional periodic conditions were consistent with the experimental density (1.0 g/cm^3) and surface area per lipid (68.1 Å^2) for a lipid/water weight ratio of 0.6 (*15*). Lipid phosphorus atoms were placed in a two-dimensional hexagonal array (36 per layer), and a series of energy minimizations eliminated any unphysically close contacts during packing (*16*). We carried out the MD simulation (with no constraints on any atom) for 190 ps (20 ps for heating and equilibration, 170 ps for analysis) at 50°C, constant particle number, volume, and energy with a time step of 0.001 ps using CHARMM [B. R. Brooks *et al.*, *J. Comput. Chem.* **4**, 187 (1983)]; approximately 15 central processor unit (cpu) hours on an IBM 3090 were required for each picosecond of simulation. The hexadecane simulation consisted of 64 molecules at a density of 0.866 g/cm^3. We developed the initial configuration by randomly packing and then energy-minimizing single chains that had been generated by Monte Carlo procedures (*13*). We carried out the simulation for 530 ps on a Hewlett Packard 730 workstation (30 ps for equilibration and 500 ps for analysis, at 3 cpu hours per picosecond), using the procedure described for the bilayer.
18. H. De Loof, S. C. Harvey, J. P. Segrest, R. W. Pastor, *Biochemistry* **30**, 2099 (1991).
19. R. W. Pastor, R. M. Venable, M. Karplus, A. Szabo, *J. Chem. Phys.* **89**, 1128 (1988).
20. D. F. Bocian and S. I. Chan, *Annu. Rev. Phys. Chem.* **29**, 307 (1978); E. Rommel, F. Noack, P. Meier, G. Kothe, *J. Phys. Chem.* **92**, 2981 (1988).
21. M. F. Brown, A. A. Ribeiro, G. D. Williams, *Proc. Natl. Acad. Sci. U.S.A.* **80**, 4325 (1983); M. F. Brown, *J. Chem. Phys.* **80**, 2808 (1984).
22. *Landolt-Bornstein Tables* (Springer-Verlag, Berlin, ed. 6, 1969), vol. II.5.
23. W. L. C. Vaz and P. F. Almeida, *Biophys. J.* **60**, 1553 (1991).
24. J. Tabony and B. Perly, *Biochim. Biophys. Acta* **1063**, 67 (1990).
25. R. M. Venable and R. W. Pastor, in preparation.
26. See (*10*), chap. 7.
27. T. M. Fischer, *Biophys. J.* **63**, 1328 (1992), and references therein.
28. We thank the Division of Computer Research and Technology at the National Institutes of Health for providing computer time on the IBM 3090; B. Brooks for technical advice as well as computer time; and A. MacKerell, M. Schlenkrick, J. Brickmann, and M. Karplus for providing a copy of PARM 22 before publication.

24 May 1993; accepted 3 August 1993

Dissipation of Marine Stratiform Clouds and Collapse of the Marine Boundary Layer Due to the Depletion of Cloud Condensation Nuclei by Clouds

Andrew S. Ackerman,* Owen B. Toon, Peter V. Hobbs

When the production of cloud condensation nuclei in the stratocumulus-topped marine boundary layer is low enough, droplet collisions can reduce concentrations of cloud droplet numbers to extremely low values. At low droplet concentrations a cloud layer can become so optically thin that cloud-top radiative cooling cannot drive vertical mixing. Under these conditions, model simulations indicate that the stratocumulus-topped marine boundary layer collapses to a shallow fog layer. Through this mechanism, marine stratiform clouds may limit their own lifetimes.

Marine stratiform clouds overlie about a third of the Earth's oceans and play a prominent role in the Earth's radiative heat balance (*1*). As shown by satellite imagery, marine stratiform clouds reflect much more sunlight than the darker underlying ocean surface and strongly enhance the Earth's global albedo (*2*). It has been estimated that the global cooling that would result from a 4% increase in the area covered by marine stratocumulus would offset the expected warming from a doubling of atmospheric carbon dioxide concentrations (*3*). Extensive sheets of marine stratocumulus are a climatological feature of the eastern regions of subtropical oceans, where the planetary boundary layer is capped by a strong temperature inversion produced by large-scale subsidence. The vertical mixing that supplies moisture to these clouds and maintains the depth of the boundary layer is generally driven by cloud-top radiative cooling (*4*). Clearly, an understanding of the processes that determine the lifetime and albedo of marine stratocumulus is of critical importance to an understanding of the Earth's climate system.

Twomey (*5*) suggested that increased numbers of cloud condensation nuclei (CCN) can enhance cloud albedo because they increase the droplet surface area for a fixed mass of cloud water. Albrecht (*6*) argued that increased CCN concentrations, which decrease cloud droplet sizes and reduce drizzle, can increase the fractional coverage of marine stratiform clouds because drizzle can regulate the liquid-water content and the lifetime of a cloud. Evidence that increases in particle concentrations can increase cloud albedo is provided by linear high-albedo cloud features over the ocean, often hundreds of kilometers long, known as "ship tracks" because they are caused by emissions from ships (*7, 8*). In this report we identify a phenomenon that is the converse of ship tracks. We have found, through numerical modeling studies, that clouds themselves may reduce particle concentrations to such an extent that the clouds dissipate and, as a consequence, the boundary layer collapses.

Variations in CCN concentrations can strongly affect cloud cover (Fig. 1). In the dark, nearly cloud-free region shown in Fig. 1, low ambient CCN concentrations were measured from aboard a ship (*8*). There were apparently not enough CCN in this dark region to maintain an optically thick cloud layer. However, a prominent cloud line (ST in Fig. 1) formed behind an underlying ship during the same period. Along this line, the injection of a large number of CCN apparently allowed a persistent cloud to form.

We suggest that drizzle in marine stratiform clouds can reduce CCN concentrations sufficiently to cause the stratocumulus-topped boundary layer to collapse to a shallow fog layer, in which cloud-top radiative cooling can no longer drive vertical mixing. A typical scenario (scenario 1) for such a collapse would be for CCN concentrations to build under cloud-free conditions. Then, when clouds form, CCN concentrations are depleted by collisions between cloud droplets that have formed on CCN and by the removal of cloud water in drizzle. The reduction in CCN concentrations can lead to the dissipation of the clouds and the collapse of the boundary layer.

We used a numerical model (*9*) to investigate this process. The production of CCN in the model was represented by a constant CCN source of 5×10^{-4} cm^{-3} s^{-1} throughout the depth of the boundary layer (*10*). The model domain was initially unsaturated and cloudless (*11*). The initial CCN concentration of 100 cm^{-3} corresponds to a constant production rate over about 2 days of cloud-free conditions in which no significant loss processes are active. Once the simulation was started, it took ~1.5 hours for a cloud layer to form (Fig. 2).

A. S. Ackerman and P. V. Hobbs, Department of Atmospheric Sciences, University of Washington, Seattle, WA 98195.
O. B. Toon, Ames Research Center, National Aeronautics and Space Administration, Moffett Field, CA 94035.

*To whom correspondence should be addressed.

The most direct and immediate response of the system to cloud formation was a decrease in CCN concentrations throughout the boundary layer. This result is reflected in the droplet concentration at cloud top (Fig. 2A), which fell from ~35 to 20 cm^{-3} after 1 day in the simulation and to 4 cm^{-3} after 2 days. As a result, the average droplet radius increased (Fig. 2B) from 17 to 19 μm in the first day and reached 30 μm after 2 days. With bigger droplets the drizzle flux increased, thereby reducing the liquid-water path (Fig. 2C). These coupled effects contributed to a 60% reduction in the cloud optical depth in 2 days (Fig. 2D).

Before the collapse, vertical mixing in the boundary layer was primarily driven by cloud-top radiative cooling, which is frequently observed (*12, 13*). The cloud layer was optically thick enough for the profile of infrared cooling to attain a pronounced maximum near cloud top. As the cloud layer became less optically thick, the peak in the cooling rate diminished and moved downward. Although infrared cooling below cloud top continued to destabilize the cloud layer with respect to the subcloud layer, it stabilized the cloud layer above the altitude of the peak cooling rate. This stabilization allowed the subsiding air to push the inversion downward, leading to the collapse of the boundary layer (Fig. 2E).

This simulated collapse of the boundary layer is not an artifact of the specified initial conditions. Cloud formation did "shock" the modeled atmosphere through the release of latent heat. To demonstrate that the collapse of the boundary layer was not simply a recovery from this shock but rather a result of an imbalance between the source and sinks of CCN, we considered a second scenario (scenario 2). In it the initial CCN production rate was four times the value used in the first scenario, which was great enough to offset the loss of CCN due to cloud processes. After 3 days, the production rate of CCN was reduced to that used in scenario 1 (corresponding to time 0), and the boundary layer collapsed in an identical manner to that obtained in the first scenario (Fig. 2). In scenario 2 there were diurnal oscillations during the 3 days preceding time 0, in which the cloud layer thickened at night and thinned during the day because of changes in vertical mixing produced by solar heating (*14*).

The albedo and infrared cooling rate of a cloud both depend on cloud optical depth (τ), which is approximated by (*15*)

$$\tau = \frac{3wh}{2r_{\mathrm{eff}}} \qquad (1)$$

where w is the average cloud liquid-water content, h is the cloud thickness, and r_{eff} is the effective radius of the cloud droplet distribution. A comparison of the changes in these parameters over 2 days (Table 1) indicates that all three parameters on the right side of Eq. 1 are of comparable significance in reducing τ (and therefore the cloud albedo). The change in τ caused the broad-band solar albedo at the top of the atmosphere to fall from 43 to 31% in 2 days (*16*). The effects on τ and cloud albedo due to changes in r_{eff} and w caused by variations in aerosol concentrations have been discussed (*5, 6*). However, the changes in τ and in cloud albedo discussed here are self-induced rather than imposed by external perturbations in CCN concentrations.

To the extent that our model represents the cloud-topped marine boundary layer, it has revealed a mechanism by which marine stratiform clouds can dissipate in addition to cloud-top entrainment instability (*17*) and decoupling between cloud and subcloud layers from solar heating (*18*). Albrecht (*6*) discussed the effect of CCN concentrations on fractional cloud amount. In his model, cloud microphysics was represented through the specification of a precipitation efficiency, assumed to be inversely related to CCN concentrations. He concluded that marine stratiform cloud coverage depends on CCN concentration because precipitation removes cloud water and reduces mixing (between the cloud and subcloud layers) through evaporation of drizzle below cloud base. Both of these mechanisms play a role in the dissipation of the cloud layer in our simulations but do not account entirely for the collapse of the boundary layer. In our simulations the main mechanism responsible for the cloud dissipation is the drastic reduction in optical depth, and the associated change in the profile of infrared cooling, that results from the coupled decreases in droplet concentration and cloud liquid-water content.

The collapse of the marine boundary layer and the associated dissipation of the marine stratiform clouds may be prevented, prolonged, or accelerated, depending on the atmospheric conditions such as the CCN production rate, initial concentration, and input size distribution, as well as the wind speed, the sea-surface temperature, and the divergence rate of the hori-

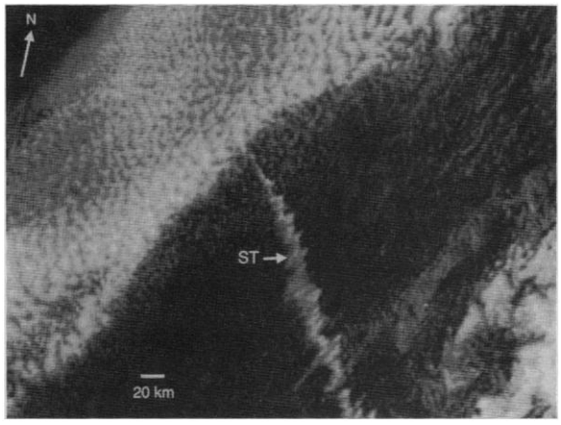

Fig. 1. Visible wavelength (0.55 to 0.75 μm) satellite image of a ship track (ST) off the coast of Southern California on 13 July 1991. The surface conditions in the vicinity of the ship track were low CCN concentrations (5 cm^{-3} at 0.8% supersaturation) and broken stratus clouds with occasional drizzle and fog. Beneath the ~18-km-wide ship track, much higher CCN concentrations (200 cm^{-3}) were measured. In the region to the northwest of the ship track, where the ship track is obscured by optically thicker stratocumulus, the ambient CCN concentrations at the surface were 60 cm^{-3} and no drizzle reached the surface. The measurements and observations are from Hindman and colleagues (*8*).

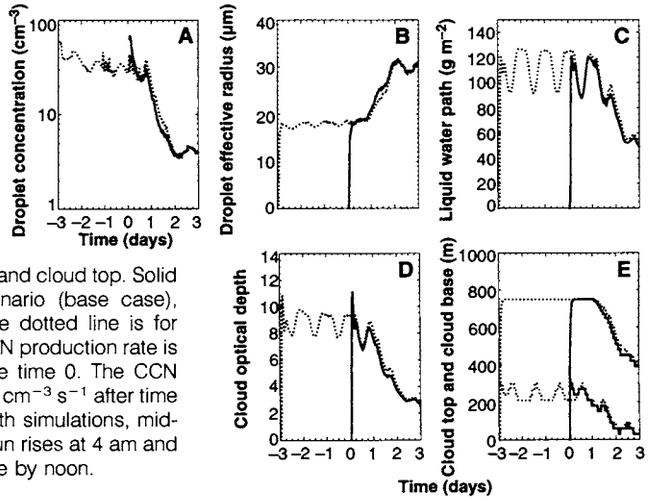

Fig. 2. Evolution of simulated cloud properties. (**A**) Droplet concentration and (**B**) droplet effective radius, both at an altitude corresponding to an optical depth of 1 below cloud top. (**C**) Cloud liquid-water path. (**D**) Optical depth of cloud. (**E**) Altitudes of cloud base and cloud top. Solid lines are for the first scenario (base case), which starts at time 0. The dotted line is for scenario 2, in which the CCN production rate is 2×10^{-3} cm^{-3} s^{-1} before time 0. The CCN production rate is 5×10^{-4} cm^{-3} s^{-1} after time 0 for both scenarios. In both simulations, midnight is at time 0 and the sun rises at 4 am and climbs to a 35° zenith angle by noon.

zontal wind velocity. We varied these conditions and repeated the scenario 1 simulation (the scenario 1 results presented above are hereafter referred to as the base case). To compare results, we defined an initial τ by its average value during the ~6-hour recovery from the shock of cloud formation and then determined a collapse time as the time it took for τ to decrease to exp (-1) of, or 0.37 times, its initial value (the *e*-folding time). Applying this definition to the base case, we found that the collapse took 45 hours, during which time the boundary layer depth decreased from 750 to 450 m.

A factor of two change in the CCN production rate strongly affected the simulated collapse of the boundary layer (Table 2). When the CCN source strength was reduced to one half of the value used in the base case, the collapse took half the time; after 45 hours the boundary layer depth decreased to 250 m. When the CCN source strength was twice that in the base case, the boundary layer did not collapse at all. In this case, the droplet number concentration declined to 11 cm^{-3} over 53 hours, r_{eff} increased to 20 μm, and the liquid-water path remained nearly constant. Apparently a threshold value for the optical depth was not reached (it fell to 6), as the vertical extent of the cloud underwent little change. When the initial CCN concentration was half that used in the base case, the collapse of the boundary layer was accelerated and intensified (Table 2). A doubling of the initial CCN concentration from the base case prolonged and weakened the collapse.

The supply of CCN from above the inversion due to subsidence can be significant (*19*). Allowing this additional CCN source to operate (with a CCN concentration above the boundary layer of 100 cm^{-3}) prevented τ from decreasing by exp (-1), although τ did fall by a factor of two (down to a value of 4) in 2 days, during which time droplet concentrations fell below 10 cm^{-3} and the boundary layer thickness fell to 530 m. When the subsidence source was doubled by an increase in the initial CCN concentration above the inversion to 200 cm^{-3}, the boundary layer did not collapse.

As an alternative to the input CCN size distribution in the base case, we considered the effect of reducing by a factor of two the mean CCN radius (by number) while doubling the breadth of the distribution. Because this change produces a reduction in peak supersaturations (more CCN nucleate droplets at low supersaturations), the initial CCN number concentration was tripled from that in the base case to produce droplet concentrations similar to those after cloud formation in the base case. With a smaller fraction of CCN nucleating droplets, their removal rate was reduced, resulting in a prolonged and weakened collapse of the boundary layer (Table 2).

Doubling of the geostrophic wind speed accelerated and slightly weakened the collapse of the boundary layer (Table 2). A higher wind shear from surface drag resulted in greater mixing, which led to increased drizzle and thereby reduced droplet concentrations faster. But because it maintained mixing, increased shear also offset some of the collapse. Another source of increased mixing is surface buoyancy. An increase in the sea-surface temperature of 3 K delayed and weakened the collapse of the boundary layer. In the first day of evolution (before droplet concentrations started to fall dramatically), the boundary layer thickness climbed to 850 m. By the time τ *e*-folded, the boundary layer thickness had decreased by 250 m, which represents a vertical collapse only 50 m less than for the base case but that results in a final boundary layer thickness 150 m greater than in the base case. Finally, an increase in the divergence rate of the horizontal wind velocity caused the boundary layer to collapse further in the same amount of time as in the base case (Table 2). Increased divergence resulted in stronger subsidence of the inversion air, which offset cloud-top radiative cooling, thereby decreasing mixing. Stronger subsidence alone would accelerate the encroachment of the inversion, but drizzle was reduced because mixing was diminished, and any potential acceleration was offset by the reduced droplet removal rate.

We do not know how often these processes result in the collapse of the marine boundary layer, but several sets of observations are consistent with its occurrence. For instance, low particle concentrations are common in the marine boundary layer (*8*, *20*). Also, the meteorological conditions under which ship tracks form correspond closely with the collapsed boundary layer that we have described (*21*). An explanation of the formation of visible ship tracks in such a boundary layer is the converse of the description of the collapse of the boundary layer described here (*22*).

Our study suggests that there is a closely coupled life cycle between CCN and stratiform clouds in the marine boundary layer. First, CCN accumulate under clean, cloud-free conditions. Clouds then form, which reduce CCN concentrations through droplet collisions. After enough time, the final stage is the collapse of the boundary layer produced by a reduction of cloud optical depth, which dissipates the clouds. Through this mechanism, marine stratiform clouds may contain the seeds of their own destruction.

Table 1. Change of cloud properties over 2 days.

Variable	Diurnal average*	Value after 2 days	Change ratio
h (m)	510	450	0.88
w (g m^{-3})	0.23	0.18	0.78
r_{eff} (μm)	18	31	0.58
τ	9.8	3.9	0.40

*The change ratio for h and w is defined as the value after 2 days divided by the diurnal average before time 0; for r_{eff} this ratio is defined as the inverse. When these definitions are combined with Eq. 1, the change ratio for τ is the product of the change ratios for the other three properties. We used the average state of the cloud before time 0 from the second scenario because it provided a more clearly defined base line than did the first scenario (Fig. 2).

Table 2. Summary of sensitivity tests. Shown for each parameter is the time after cloud formation for the total optical depth to *e*-fold and the boundary layer thickness at that time. The absence of a value indicates that the boundary layer did not collapse.

Parameter	Base case value*	Sensitivity value	Time for τ to *e*-fold (hours)	Boundary layer thickness (m)
CCN production rate (cm^{-3} s^{-1})	5×10^{-4}	2.5×10^{-4}	27	450
CCN production rate (cm^{-3} s^{-1})	5×10^{-4}	1×10^{-3}		
CCN initial concentration (cm^{-3})	100	50	39	380
CCN initial concentration (cm^{-3})	100	200	53	560
Geometric SD of CCN size distribution	1.2	2.5	49	530
Subsidence CCN source (cm^{-3} s^{-1})	0	3×10^{-4}		510†
Subsidence CCN source (cm^{-3} s^{-1})	0	6×10^{-4}		
Geostrophic wind speed (m s^{-1})	5	10	40	470
Sea-surface temperature (K)	288	291	52	600
Divergence rate of horizontal wind (s^{-1})	3×10^{-6}	5×10^{-6}	45	400

*In the base case, the time to *e*-fold was 45 hours and the boundary layer thickness at that time was 450 m. †Value when τ fell by a factor of 2 (after 49 hours).

REFERENCES AND NOTES

1. S. G. Warren, C. J. Hahn, J. London, R. M. Chervin, R. L. Jenne, *Global Distribution of Total Cloud Cover and Cloud Type Amounts over the Ocean* (National Center for Atmospheric Research, Boulder, CO, 1988), p. 34.
2. The global albedo is the fraction of incident (shortwave) solar radiation reflected by the Earth. Because low-lying clouds radiate to space at a temperature near that of the ocean surface, their impact on the global longwave radiation budget is small.
3. D. A. Randall, J. A. Coakley, C. W. Fairall, R. A. Kropfli, D. H. Lenschow, *Bull. Am. Meteorol. Soc.* **65**, 1290 (1984).

4. D. K. Lilly, *Q. J. R. Meteorol. Soc.* **94**, 292 (1968).
5. S. Twomey, *Atmos. Environ.* **8**, 1251 (1974).
6. B. A. Albrecht, *Science* **245**, 1227 (1989).
7. J. H. Conover, *J. Atmos. Sci.* **23**, 778 (1966); J. A. Coakley, Jr., R. L. Bernstein, P. A. Durkee, *Science* **237**, 1020 (1987); L. F. Radke, J. A. Coakley Jr., M. D. King, *ibid.* **246**, 1146 (1989); M. D. King, L. F. Radke, P. V. Hobbs, *J. Geophys. Res.* **98**, 2729 (1993).
8. E. E. Hindman, W. M. Porch, J. G. Hudson, P. A. Durkee, in *Proceedings of the 11th International Conference on Clouds and Precipitation*, Montreal, Canada, 17 to 21 August 1992 (Department of Meteorology, McGill University, Montreal, Canada), pp. 184–187.
9. The cloud microphysical model [O. B. Toon, R. P. Turco, D. Westphal, R. Malone, M. S. Liu, *J. Atmos. Sci.* **45**, 2123 (1988)] resolves the distributions of both unactivated CCN and cloud droplets and explicitly treats the warm cloud microphysical processes that affect them. Vertical transport is represented with a turbulent kinetic energy closure scheme [P. G. Duynkerke and A. G. M. Driedonks, *ibid.* **44**, 43 (1987)]. The model uses the radiative transfer scheme of O. B. Toon, C. P. McKay, T. P. Ackerman, and K. Santhanam [*J. Geophys. Res.* **94**, 16287 (1989)].
10. Similar values were estimated by others to be an average CCN production rate [M. B. Baker and R. J. Charlson, *Nature* **345**, 142 (1990); D. A. Hegg, *Geophys. Res. Lett.* **17**, 2165 (1990)]. The distribution of CCN is specified as log-normal with a (number) mean radius of 0.1 μm and a geometric SD of 1.2, similar to surface measurements from the remote, cloud-free Pacific Ocean [A. D. Clarke, N. C. Ahlquist, D. S. Covert, *J. Geophys. Res.* **92**, 4179 (1987)]. Another potential source of CCN, due to subsidence of air from above the boundary layer, was included in sensitivity tests. The constant CCN production rate does not include the possibility that CCN production is favored when particle concentrations are low [X. Lin, W. L. Chameides, C. S. Kiang, A. W. Stelson, H. Berresheim, *J. Geophys. Res.* **97**, 18161 (1992)].
11. The initial temperature profile was adiabatic up to 750 m, where there were jumps in temperature (+6 K) and water vapor (-2 g kg^{-1}). The sea-surface temperature was fixed at 288 K. The downwelling infrared flux at the top of the model (at a height of 1 km) was fixed at 270 W m^{-2}, and the wind speed in the top layer of the model was fixed at the geostrophic value of 5 m s^{-1}. The divergence rate of horizontal wind velocity was constant at 5×10^{-6} s^{-1}.
12. S. Nicholls, *Q. J. R. Meteorol. Soc.* **110**, 783 (1984).
13. S. Nicholls and J. Leighton, *ibid.* **112**, 431 (1986).
14. Solar heating offsets infrared cooling and stabilizes the temperature profile between the cloud and subcloud layers, leading to a decoupling in vertical mixing between the layers (*12*).
15. In Eq. 1 it is assumed that the cloud droplet size distribution is vertically uniform [J. E. Hansen and L. D. Travis, *Space Sci. Rev.* **16**, 527 (1974)]. However, the modeled cloud droplet size distributions varied with height in the cloud. Therefore, we determined an optically representative value of r_{eff} by evaluating it at an altitude corresponding to an optical depth of 1 below cloud top. At time 0 in the second scenario this optically representative altitude occurred 50 m below cloud top; after 2 days this altitude descended to 100 m below cloud top. Values of τ given in Table 1 are calculated from Eq. 1 and are within ~10% of the optical depth calculated by the integration of extinction coefficients over the profile of droplet size distributions (Fig. 2D). Cloud thickness is taken to be the difference between the altitudes at which visibility is <1 km. The average liquid-water content is calculated by dividing the vertically integrated liquid-water path by *h*.
16. For this comparison, calculations of the albedo at the top of the atmosphere were made at a constant solar zenith angle of 60°. The cloud-free albedo in the model was 12%.
17. In the diurnal average of scenario 2 before time 0, there are differences between the above-cloud values and the cloud-top values of +2 K in equivalent potential temperature and -2 g kg^{-1} in the total water mixing ratio. Therefore, cloud-top entrainment instability could not have occurred in our simulations [D. A. Randall, *J. Atmos. Sci.* **37**, 125 (1980); H. Kuo and W. H. Schubert, *Q. J. R. Meteorol. Soc.* **114**, 887 (1988); M. K. MacVean and P. J. Mason, *J. Atmos. Sci.* **47**, 1012 (1990)].
18. Solar heating has been suggested as a precursor to the breakup of marine stratiform clouds by D. P. Rogers and D. Koracin [*J. Atmos. Sci.* **49**, 1473 (1992)]. Although the cloud dissipation shown in Fig. 2 occurred near sunrise, this was coincidental. A variation on our second scenario in which the reduction to the lower CCN production rate was delayed 12 hours led to a collapse of the boundary layer that was also delayed by 12 hours.
19. Averaged over the depth of the boundary layer, the particle source due to subsidence is the product of the divergence rate and the concentration of CCN above the boundary layer. A divergence of 3×10^{-6} s^{-1} and a CCN concentration of 100 cm^{-3} provide 3×10^{-4} particles per cm^3 per s to the boundary layer.
20. S. Twomey, H. B. Howell, T. A. Wojciechowski, *J. Atmos. Sci.* **25**, 333 (1968); D. A. Hegg, R. J. Ferek, P. V. Hobbs, L. F. Radke, *J. Geophys. Res.* **96**, 13189 (1991); D. A. Hegg, L. F. Radke, P. V. Hobbs, *ibid.*, p. 18727.
21. C. J. Bowley, *J. Atmos. Sci.* **24**, 596 (1967).
22. A strong injection of CCN under these conditions would cause an increase in droplet concentrations. This would lead to a reduction in droplet sizes, which would cause a decrease in drizzle, allowing an increase in cloud liquid water. The ultimate result, the triggering of a visible ship track, would be an enhancement of cloud optical depth substantial enough to drive vertical mixing through cloud-top radiative cooling.

23. This work was supported by the National Aeronautics and Space Administration (NASA), the U.S. Department of Energy, and the National Science Foundation. Computations were performed at the Numerical Aerodynamic Simulation Program facility at NASA Ames Research Center.

20 April 1993; accepted 20 August 1993

High-Temperature XAS Study of Fe_2SiO_4 Liquid: Reduced Coordination of Ferrous Iron

W. E. Jackson,* J. Mustre de Leon, G. E. Brown Jr.,† G. A. Waychunas, S. D. Conradson, J.-M. Combes

X-ray absorption spectroscopy (XAS) of Fe^{2+} in Fe_2SiO_4 liquid at 1575 kelvin and 10^{-4} gigapascal (1 bar) shows that the Fe^{2+}–O bond length is 1.98 ± 0.02 angstroms compared with ≈2.22 angstroms in crystalline Fe_2SiO_4 (fayalite) at the melting point (1478 kelvin), which indicates a decrease in average Fe^{2+} coordination number from six in fayalite to four in the liquid. Anharmonicity in the liquid was accounted for using a data analysis procedure. This reduction in coordination number is similar to that observed on the melting of certain ionic salts. These results are used to develop a model of the medium-range structural environment of Fe^{2+} in olivine-composition melts, which helps explain some of the properties of Fe_2SiO_4 liquid, including density, viscosity, and the partitioning of iron and nickel between silicate melts and crystalline olivines. Some of the implications of this model for silicate melts in the Earth's crust and mantle are discussed.

Ferrous iron (Fe^{2+}) is the major transition metal in mafic and ultramafic silicate melts in the Earth's lower crust and upper mantle (*1*) and in some metallurgical slags. In such liquids, Fe^{2+} is commonly believed to be six-coordinated by oxygens (*2*), but it might be four- or five-coordinated as well (*3, 4*). Such differences in iron coordination would have a significant effect on the physical properties of these liquids, particularly on their density, viscosity, and ionic diffusivity, because of expected increases in metal-oxygen bond strength with decreasing coordination number and bond length. Thus, knowledge of the local coordination environment of Fe^{2+} in silicate liquids as a function of temperature is necessary to understand these and other properties and to help constrain models of Earth's partially molten interior (*5*).

There is little direct information about the coordination environments of transition metals in silicate liquids because structural studies of liquids at temperatures >1000 K are experimentally difficult and techniques such as nuclear magnetic resonance (NMR) and Raman spectroscopy, which have provided valuable information on the polymeric structure of silicate liquids, are not well suited for studies of transition-metal environments. Most information on the effects of temperature, pressure, and composition on the structure of such melts, including the coordination environment of transition metals, has been derived by inference and extrapolation from

W. E. Jackson and G. E. Brown Jr., Department of Geological and Environmental Sciences and Stanford Synchrotron Radiation Laboratory, Stanford University, Stanford, CA 94305.
J. Mustre de Leon and S. D. Conradson, Electronics Research Group, Los Alamos National Laboratory, Los Alamos, NM 87545.
G. A. Waychunas, Center for Materials Research, Stanford University, Stanford, CA 94305.
J.-M. Combes, St. Gobain Inc. Recherche, 93304 Aubervilliers, France.

*Present address: General Electric Company, 6325 Huntley Road, Post Office Box 568, Worthington, OH 43085.
†To whom correspondence should be addressed.